

Combined Impedance and Electron Paramagnetic Resonance Spectroscopy for Investigating the Dynamics of Li/Solid Li-ion Conductor Interfaces

Rainer Götz,^[a] Michael Wagner,^[a] Kun-Ting Song,^[a] Leon Katzenmeier,^[a] and Aliaksandr S. Bandarenka^{*[a]}

Electrochemical impedance spectroscopy (EIS) is a widely used tool for the electrochemical characterization of all-solid-state batteries (ASSBs) with Li-metal anodes. However, an unambiguous interpretation of the observed impedance response often requires additional independent information on the actual interfacial phenomena obtained. The measurement methodology presented in this study allows to conduct electron paramagnetic resonance (EPR) spectroscopy and EIS concurrently. Therefore, the informative power of EIS experiments can be significantly improved *via* monitoring of structural changes of paramagnetic lithium at the electrochemical interface. As the solid-electrolyte-lithium interface is a critical part of all-solid-state batteries, this study employs a model oxide solid electro-

lyte in contact with lithium metal. During the polarization of the cell with thin evaporated lithium electrodes, the ratio between positive and negative peaks (a/b) of the EPR signal momentarily rises, which indicates an accumulation of lithium on one side of the electrolyte. The peak ratio a/b then drops abruptly, accompanied by current irregularities. Both are indicative of a diminishing contact area, and as a result, finer lithium morphologies form. Shortly after that, a contact loss is observed. The change of the EPR signal shape before cell breakdown can hence be associated with the worsening Li-electrolyte contact, providing a tool for physical *in-situ* cell diagnostics.

Introduction

In battery research, electrochemical impedance spectroscopy (EIS) is the most established experimental technique, as it allows the deconvolution of bulk mass transport and interfacial charge transfer. Electron paramagnetic resonance (EPR) spectroscopy is less used in this field, although it can provide valuable additional information about the systems. For example, most cathode materials include transition metals, which change their oxidation state upon lithium de-/intercalation. As EPR measures unpaired electron spins, the materials typically either become EPR-active or silent, depending on their oxidation state. Additionally, paramagnetic species can be formed as defects during degradation.^[1–3] Secondly, lithium metal represents a special case of EPR as the effects of conduction-EPR (CEPR) are highly dependent on lithium dimensions, especially compared to its skin depth.^[4–6] The skin depth is material-specific and indicates the depth to which spins can still be fully excited from the magnetic field and, hence, contribute to the signal. For lithium metal, this thickness can be calculated to be around 1.1 μm.^[7] The relation between the skin depth and the sample thickness

allows CEPR to associate a certain lithium morphology with the recorded EPR line shape. Hence, the more asymmetric the EPR signal gets, i.e., the bigger the ratio of the peak heights (a/b) becomes, the thicker the lithium dimensions (Figure 1).^[7,8]

While this relationship has already been established for lithium-ion batteries with liquid electrolytes, where the structural changes upon continuous lithium plating/stripping can be observed,^[7–11] relatively little research has been done similarly

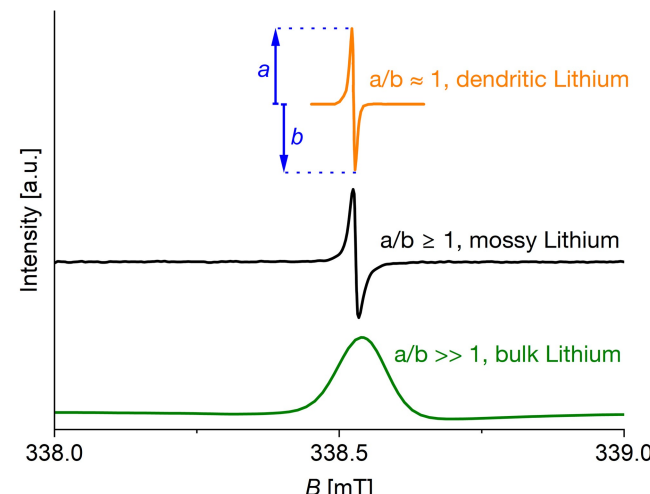


Figure 1. Relation between EPR signal and lithium morphology. Lithium structure can be distinguished by the ratio of positive peak height a to negative peak height b , as well as the peak width. Signal shapes like the one for dendritic lithium are called Lorentzian, and bulk lithium shows a Dysonian EPR signal. Reproduced with permission from Ref.^[7]

[a] R. Götz, M. Wagner, K.-T. Song, L. Katzenmeier, A. S. Bandarenka
Physics of Energy Conversion and Storage, Department of Physics, Technical University of Munich, James-Franck-Str. 1, 85748 Garching, Germany
Tel. +49 (0) 89 289 12531
E-mail: bandarenka@ph.tum.de

© 2024 The Author(s). *Batteries & Supercaps* published by Wiley-VCH GmbH.
This is an open access article under the terms of the Creative Commons Attribution License, which permits use, distribution and reproduction in any medium, provided the original work is properly cited.

for the emerging all-solid-state batteries (ASSBs).^[12,13] ASSBs are claimed to be safer (non-flammable), energy denser (by allowing high-capacity lithium metal anodes), and are expected to enable ultrafast charging (due to, e.g., better thermal conductivity).^[14] So far, one cannot speak of broad commercialization given the few fully functioning prototype cells present.^[15,16] Possible reasons lie in the transition to full solid-state chemistry, where the mentioned advantages can be achieved, but at the same time, new issues arise from the physicochemical challenges around the solid electrolyte and its interfaces.^[12]

In this work, we use the LICGC™ (Lithium-Ion Conducting Glass Ceramic) NASICON-type ceramic electrolyte with the ionic conductivity of $1 \cdot 10^{-4}$ S/cm from OHARA Inc.^[17] This electrolyte has already been investigated with various metal electrodes in blocking conditions as well as at varying temperatures.^[18] The NASICON-type electrolytes are a group of materials known to include stiff and, hence, supposedly dendrite-preventive ceramics,^[19] but they are also prone to chemical instability^[20] upon contact with metallic lithium. Moreover, the mechanical contact is an issue at the interface,^[21] even if the surface is as well-polished as it is for the LICGC™.^[22]

Impedance measurements are a common investigation method for battery materials and their interfaces. However, although the stability of an all-solid-state cell can be assessed with EIS, the main reasons why the solid-electrolyte-lithium interface degrades cannot be deducted from impedance data alone. For example, EIS typically cannot determine the contribution of a changing lithium morphology on a degrading physical contact between the Li(s)-anode and the solid electrolyte. In contrast, EPR spectroscopy can provide this information if the lithium properties change during *in-situ* measurements. So far, electrochemical impedance investigations that additionally use *in-situ* EPR measurements are rare and, if available, feature liquid electrolytes. Hence, this work looks at the stability issues at the solid-electrolyte-lithium interface to link degradation to the responses of EIS as well as EPR spectroscopy.

Experimental

Electrochemical Impedance Spectroscopy

Impedance measurements were carried out by a VSP300 potentiostat from Biologic (France). A perturbation amplitude of 10 mV was used for all impedance measurements, and the probing frequencies range between 3 MHz and 1 Hz. Potentiostatic impedance spectra were conducted between -1.0 V and $+1.0$ V vs. Li with a step size of 0.2 V. Potentials were kept for 15 mins, during which EPR spectra were recorded. The exact order was the following: 0 V → -1 V → $+1$ V → 0 V, while the analyzed data stems from the -1 V → $+1$ V pass. All measurements were performed at room temperature.

Electron Paramagnetic Resonance Spectroscopy

EPR spectra were recorded on a CW-EPR 'SpinScanX' spectrometer from LINEV ADANI (Belarus). A modulation frequency of 100 kHz was used for all described experiments. The parameters for the EPR measurement are the following: modulation amplitude 50 μ T,

sweep time 60 s, microwave power 1 mW, microwave frequency 9.386 GHz. After assembly in the Argon-filled glovebox ($O_2 < 0.5$ ppm, $H_2O < 0.5$ ppm), the cells were sealed to ensure an inert atmosphere and transferred to the EPR spectrometer. At each potential step, a few spectra were taken for the *in-situ* EPR measurements of the Li/LICGC™/Li cells.

Preparation of ASSB Cells

While Niemöller^[7] and Szczuka^[10] used a custom-manufactured quartz glass cell for their studies on metallic lithium morphology in liquid electrolytes, this study examines the feasibility of 3D-printed cells for an all-solid-state system. Both of the most common additive manufacturing materials, PLA (polylactic acid) and ABS (acrylonitrile butadiene styrene), are EPR-silent, and since temperature resistance is not explicitly needed, PLA was chosen.^[23] Substrates were printed out of PLA and then either covered by lithium through thermal evaporation with a *Mini Coater* (tectra GmbH, Germany) or metallic lithium sheets were cut to suitable sizes (Figure 2A). The electrolyte shards between both substrates were around 0.3 cm^2 for both evaporated and bulk lithium metal (Figure 2B). Copper stripes act as a contact to both lithium electrodes.

A 3D-printed wiring support (made from ABS) guides the copper strings upwards of the EPR tube. At the very top, electrical wires are attached and fit through two holes in the EPR cap. The assembled cells (bulk and thin lithium) are transferred into quartz EPR tubes with a 9 mm inner diameter. Impedance tests ensured that contact was established. A rubber cap with two holes for the electrical wiring closes the cell. The holes were sealed with a two-component epoxy glue (UHU®). Additionally, Parafilm® tape (Bemis, USA) is wrapped around the cap to improve the cell sealing (Figure 2C). One Li(s)-electrode connects to the working electrode (WE) while the other side acts as both counter (CE) and reference electrode (RE).

As a reference, a full-sized cell is assembled with a LICGC™ disc of 19 mm diameter, and metallic lithium chips (15 mm diameter, Mateck) were attached to both sides (Figure 3A). The reference setup remained in the glovebox within a 'PAT-cell' (EL-CELL, Germany).

Results and Discussion

Since the available space is limited to a cylindrical EPR tube with a 9 mm inner diameter, the cells must be miniaturized to fit in this confined space. Hence, in order to compare cells with different contact areas, the ionic conductivity of $\sim 1 \cdot 10^{-4}$ S/cm given by the manufacturer^[17] serves as a reference point. With the measured resistance of the bulk, one can calculate an apparent electrolyte conductivity using the following equation:

$$\sigma_{app} = \frac{d}{R_b A}$$

where d is the thickness (150 μ m), R_b is the measured bulk resistance, and A is the contact area between the electrolyte and lithium. The reference Li/LICGC™/Li-cell yields an apparent conductivity of $\sim 4.2 \cdot 10^{-5}$ S/cm. Despite the stack pressure of around 3 bar, which the 'PAT-cell' can provide, the difference in ionic conductivity already hints at mechanical contact issues at

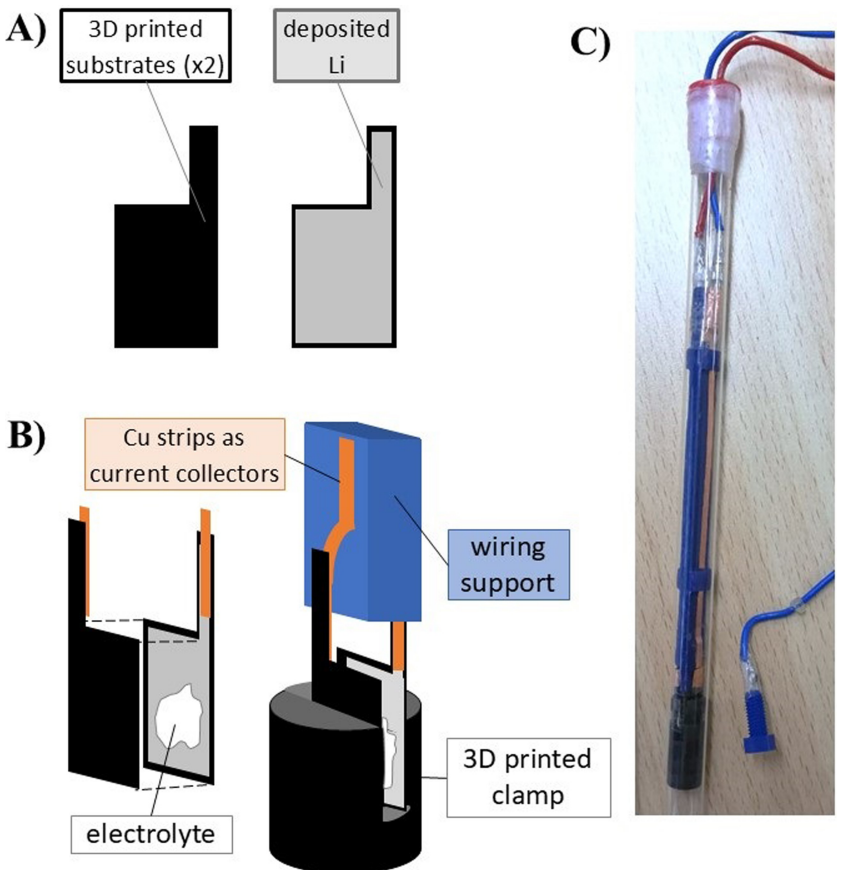


Figure 2. Assembly of 3D-printed cells. (A) Substrates are 3D-printed and either are coated by evaporating lithium onto them or metallic lithium is cut into shape. (B) Two substrates with a LICGC™ shard in between are put together and fixated by a clamp. Copper strips act as current collectors and are guided along the 3D-printed wiring support. (C) Assembled cell in a 9 mm EPR tube.

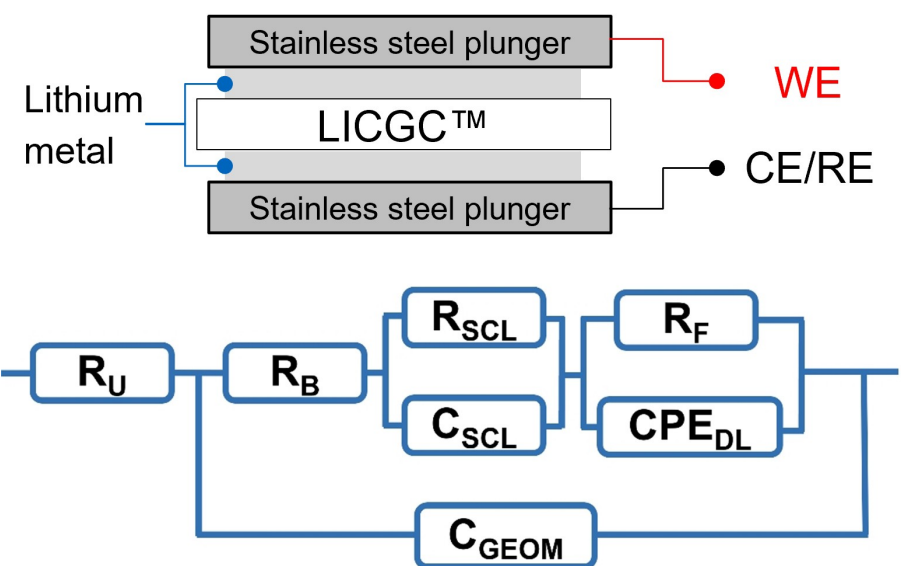


Figure 3. (A) 2-electrode cell setup for the reference cell in a 'PAT cel'. (B) Equivalent circuit for the LICGC™ electrolyte under non-blocking conditions^[20,24]. R_u – uncompensated resistance, R_b – resistance of the bulk electrolyte, R_{SCL}/C_{SCL} – resistance and capacitance of the depletion space charge layer. CPE_{DL} – constant phase element describing the response of the double layer, R_f – faradic resistance, and C_{GEOM} – geometric capacitance of the cell.

the interface. The spectra of both miniaturized cells can be fitted with the adopted model proposed by Katzenmeier

et al.^[16,25] (Figure 3B) with low root-mean-squared deviations and low estimated individual parameter errors, as shown in Figure 4.

The bulk lithium assembly had an apparent electrolyte conductivity of $\sim 6.4 \cdot 10^{-6}$ S/cm, and the interface resistances were at the same time very high (Table 1: R_F and R_{SCL}). Also, the contact turned out to be unstable. However, the cell with evaporated lithium proved to be more stable over time and showed lower impedance values than bulk lithium (Figure 4B). The calculated apparent conductivity of the electrolyte of $2.8 \cdot 10^{-5}$ S/cm comes close to the value of the reference cell, indicating an adequate physical contact between evaporated lithium and electrolyte. Still, the contact worsens, as the second semicircle increases with each measured spectrum. Besides electrolyte degradation due to direct contact with metallic lithium, minimal cell leakage cannot be entirely excluded.

From here on, the results obtained with evaporated lithium are discussed, from which most likely all of the paramagnetic lithium within the cavity dimension should contribute to the EPR signal since both deposited thicknesses are below the lithium skin depth. The ratio between the positive peak a and negative peak b (both with respect to the baseline) of the EPR

Table 1. Impedance analysis for the reference cell, and both bulk and evaporated lithium cells for the first impedance spectrum after assembly.

	Reference cell	Evaporated lithium, in-situ cell	Bulk lithium, in-situ cell
Area [mm ²]	177	ca. 30	ca. 30
R_B [kΩ]	0.2	1.8	7.8
R_F [kΩ]	6.0	25	$29 \cdot 10^2$
R_{SCL} [kΩ]	5.9	2.0	$1.9 \cdot 10^4$
C_{GEOM} [nF/cm ²]	0.8	0.4	0.2
CPE_{DL} [nF ⁿ⁻¹ /cm ²]	255	16	13
C_{SCL} [nF/cm ²]	18	0.6	5.0
n	0.7	0.8	0.8

signal is plotted in the top half of Figure 5A to evaluate the changes with respect to the applied potential.

The EPR spectra recorded during the 15-min-long potentiostatic steps all show a slightly asymmetric signal shape. From the start of the measurement at -1.0 V, the a/b ratio is

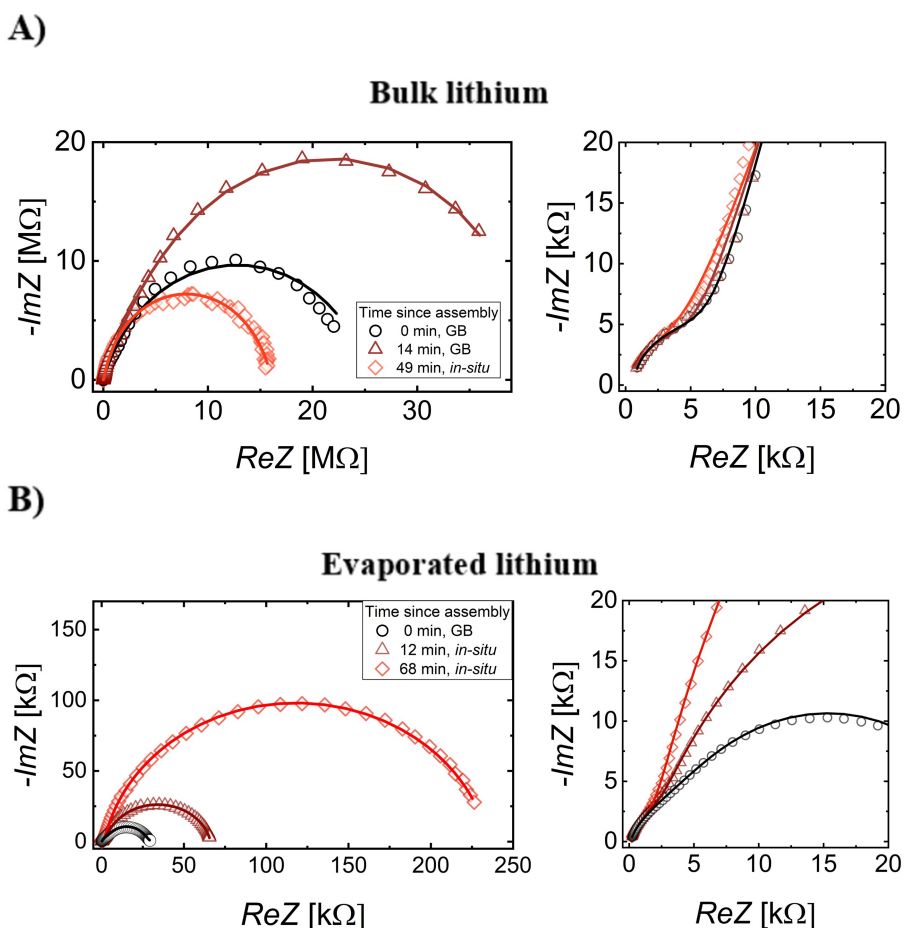


Figure 4. Impedance spectra of the Li-cell at 0 V vs. Li/Li⁺ with (A) bulk and (B) thin lithium electrodes, respectively. The whole frequency range (left) and high frequencies (right). Legend: GB measured in the glove box; in-situ: measured in the EPR spectrometer. Solid lines are fits with the EEC shown in Figure 3C. Measured frequencies: 3 MHz–1 Hz (bulk lithium) and 3 MHz–100 Hz (evaporated lithium).

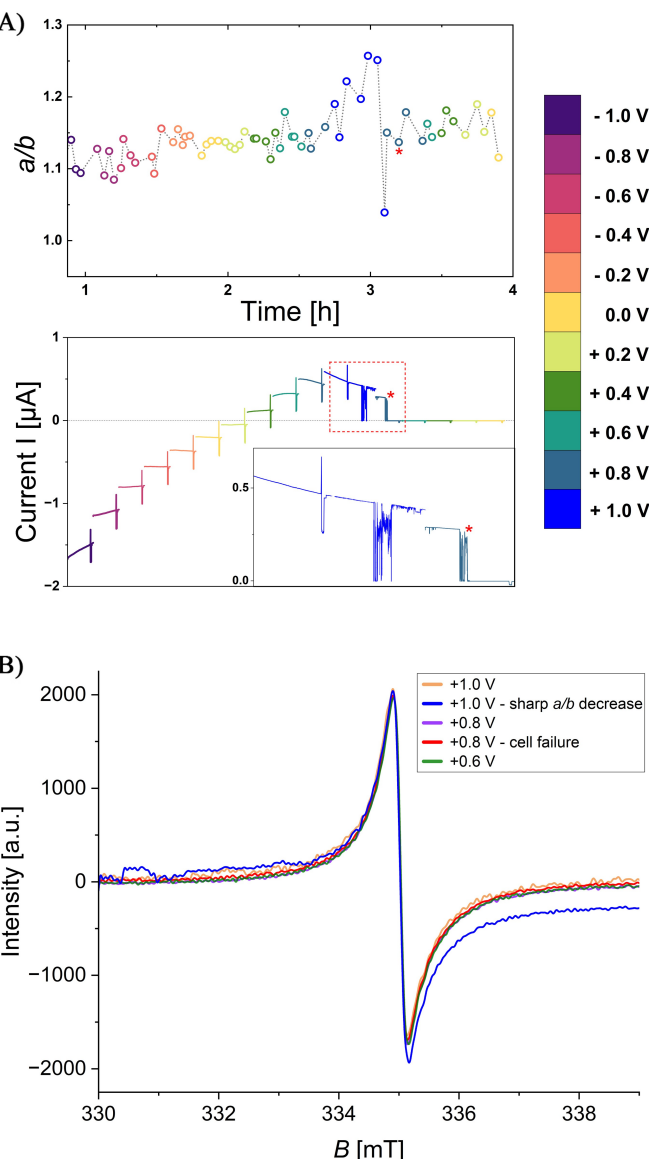


Figure 5. In-situ EC-EPR measurements (A) Top: Peak ratio a/b of recorded EPR spectra over time of the thin lithium cell. Dashed lines are just a guide for the eye. Bottom: Recorded current during potential holds, including irregularities in the current at $+1.0$ V, coinciding with the a/b drop, see inset for a zoom of the region marked by the red rectangle. At contact loss, the current drops to zero. Asterisks mark measurements or point at cell breakdown. The peak at the end of each potentiostatic step represents the point where an impedance measurement starts. (B) Selected EPR spectra before, at, and after cell failure in chronological order.

relatively constant. Then the line shape becomes slowly more asymmetric, as the a/b ratio increases towards $+1.0$ V, only to drop to a minimum for the last EPR spectrum at $+1.0$ V. In the bottom half of Figure 5A, the correspondingly colored current profiles are depicted, which are recorded during the potentiostatic steps. While during the increase of the a/b ratio, the current profile does not show anything abnormal, the sudden decrease in a/b corresponds with the occurrence of irregularities in current (inset), followed by a drop to zero current at $+0.8$ V (marked with a red asterisk). Additionally, Figure 5B

depicts spectra around cell failure and shows the sudden change in signal shape shortly before the contact loss.

As applying a potential to the cell causes lithium stripping on one side of the solid electrolyte and lithium plating on the opposite side, the thickness of the lithium on the latter side has increased, approaching skin depth. As can be seen in Figure 1, the bigger the dimensions of the lithium structures are, from dendritic to bulk, the higher the peak differences, and the EPR signal tends towards a more asymmetric shape.^[3] Hence, an increasing a/b ratio indicates accumulating lithium on one side.

It is necessary to consider the dynamic change at the interface to interpret such a behavior. As Kasemchainan et al.^[26] describe, the critical current density for lithium plating and stripping determines how fast void and dendrite formation progresses. Also, voids, once formed during the first polarization (here negative potentials), may improve momentarily after reversing polarization, which is indicated by a decreasing R_B up to $+0.4$ V.

The conductivity of the electrolyte at this point is $3.2 \cdot 10^{-4}$ S/cm and, therefore, not only surpasses the value of the reference cell but also the one reported by the manufacturer. This cannot only be attributed to the improved contact but also has been shown to originate from a Li-enriched electrolyte.^[24,27,28] At the same time, voids start to form on the other side of the solid electrolyte, diminishing the contact area. As a result, R_B increases again (Figure 6A). The same goes for C_{GEOM} , as the measurement of both bulk features depends on the contact area. At the interface, the impedance parameters from the double layer show a minimal capacitance at $+0.4$ V, associated with the constant phase element (n value: 0.77). Consequently, the double layer is the thickest, and, accordingly, the faradaic resistance is the highest (Figure 6B). The interpretation of the (depletion) space charge layer impedance during such dynamic changes at the interface is not trivial, as for an accurate assessment, the interface should be as smooth as possible. However, the surge in R_{SCL} from $+0.4$ V on, along with the sudden decrease in C_{SCL} (Figure 6C), can be another indication of the increasingly rough interface between lithium metal and solid electrolyte.

Finally, shortly before contact loss, the EPR signal deviates from the rest, as the contact area becomes minimal and the local current density can surge, leading to the formation of mossy or dendritic lithium. The a/b ratio supports this, as the smaller the lithium morphology gets, the more Lorentzian the signal becomes, and, hence, the ratio goes towards unity (cf. Figure 1).^[7] The EPR data can, therefore, be seen as a physical indicator that predicts the coming cell failure.

Nevertheless, it does not explain why the EPR signal would have such a behavior only for a very limited time (Figure 5B). However, Hartmann et al.^[18] show that the decomposition of the electrolyte includes the reduction of, e.g., Ti_2O_3 and GeO_2 , due to metallic lithium, while Li itself turns into EPR-silent Li_2O . Hence, fine-structured lithium at the interface may undergo a similar transition to explain the quick disappearance of the respective EPR feature. This hints at the fact that the formation of mossy/dendritic lithium metal leads to even faster chemical

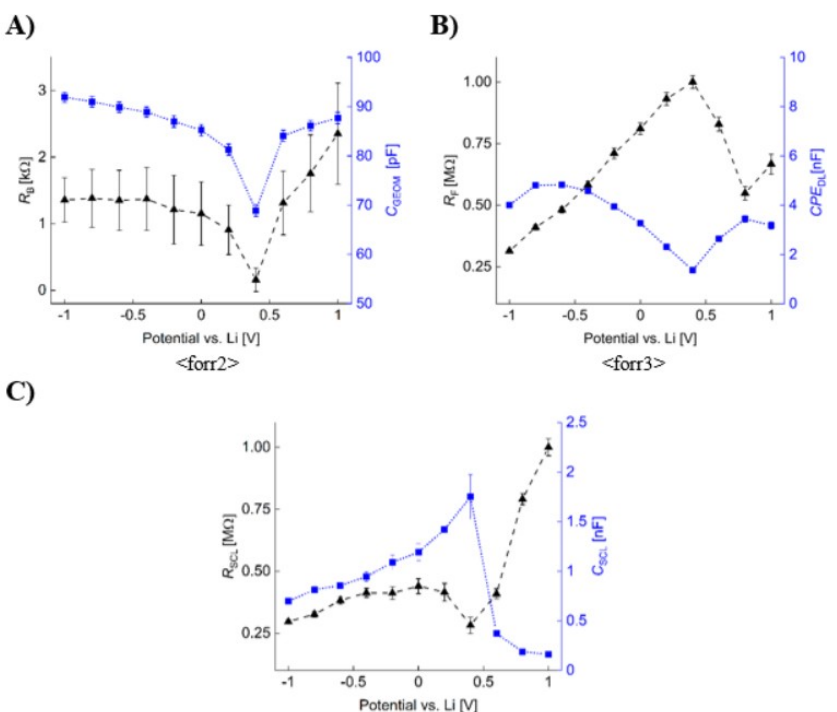


Figure 6. Impedance analysis of the thin lithium cell during the in-situ EPR measurements, from -1 V to $+1\text{ V}$. (A) Bulk resistance R_B and geometric capacitance C_{GEOM} (B) faradaic resistance R_F and double layer capacitance CPE_{DL} and (C) depletion space charge layer resistance R_{SCL} and capacitance C_{SCL} .

degradation of the interface, linked to the physical changes at the Li/electrolyte interface.

Conclusions

The measurement methodology presented in this study enables concurrent electron paramagnetic resonance spectroscopy and electrochemical impedance spectroscopy, significantly enhancing the informative power of impedance experiments by monitoring structural changes in paramagnetic lithium at the electrochemical interface. As the solid-electrolyte-lithium interface is pivotal in all-solid-state batteries, our study employs a model oxide solid electrolyte, LICG™, in contact with lithium metal. This work also introduces an EPR setup featuring a flexible, EPR-silent, and 3D-printed cell geometry explicitly designed for all-solid-state battery cells, and using evaporated thin lithium rather than bulk lithium metal results to improve stability and lower interfacial impedance. During the polarization of thin lithium cells, EIS detects a loss of contact, while EPR reveals intriguing dynamics: Before the contact loss, the a/b ratio of the EPR signal transiently rises, suggesting lithium accumulation on one side of the electrolyte. Subsequently, the abrupt drop in the a/b ratio accumulation indicates the formation of finer lithium morphologies due to decreasing contact area and the following rapid increase in local current density, ultimately leading to cell failure. The simultaneously recorded irregular current profile underlines the worsening contact. This correlation between EIS and EPR data provides valuable insights into in-situ cell diagnostics, as well as under-

scores the mechanical challenges at the interface between electrolytes and lithium metal, highlighting its significance not only in liquid but also for all-solid-state battery systems.

Acknowledgements

We gratefully thank the financial support from the Deutsche Forschungsgemeinschaft (DFG) under Germany's excellence strategy – EXC 2089/1 – 390776260, Germany's excellence cluster "e-conversion". Open Access funding enabled and organized by Projekt DEAL.

Conflict of Interests

The authors declare no conflict of interest.

Data Availability Statement

The data that support the findings of this study are available from the corresponding author upon reasonable request.

Keywords: ASSB • EPR spectroscopy • Impedance spectroscopy • Lithium metal • Interfaces

- [1] W. El Mofid, S. Ivanov, A. Konkin, A. Bund, *J. Power Sources* **2014**, *268*, 414–422.

- [2] T. Li, X. Z. Yuan, L. Zhang, D. Song, K. Shi, C. Bock, *Electrochem. Energy Rev.* **2020**, 3(1), 43–80.
- [3] A. Niemöller, P. Jakes, R. A. Eichel, J. Granwehr, *Chem. Phys. Lett.* **2019**, 716, 231–236.
- [4] B. M. Khabibullin, É. G. Kharakhash'yan, *Adv. Phys. Sci.* **1974**, 16(6), 806.
- [5] F. J. Dyson, *Phys. Rev.* **1955**, 98(2), 349.
- [6] G. Feher, A. F. Kip, *J. Exp. Phys. Rev.* **1955**, 98(2), 337.
- [7] A. Niemöller, P. Jakes, R. A. Eichel, J. Granwehr, *Sci. Rep.* **2018**, 8(1), 1–7.
- [8] J. Wandt, C. Marino, H. A. Gasteiger, P. Jakes, R. A. Eichel, J. Granwehr, *Energy Environ. Sci.* **2015**, 8(4), 1358–1367.
- [9] C. E. Dutoit, M. Tang, D. Gourier, J. M. Tarascon, H. Vezin, E. Salager, *Nat. Commun.* **2021**, 12(1), 1–6.
- [10] C. Szczuka, J. Ackermann, P. P. M. Schleker, P. Jakes, R. A. Eichel, J. Granwehr, *Commun. Mater.* **2021**, 2(1), 1–7.
- [11] F. Geng, Q. Yang, C. Li, M. Shen, Q. Chen, B. Hu, *Chem. Mater.* **2021**, 33(21), 8223–8234.
- [12] M. Li, J. E. Frerichs, M. Kolek, W. Sun, D. Zhou, C. J. Huang, & P. Bieker, *Adv. Funct. Mater.* **2020**, 30(14), 1910123.
- [13] Y. Jiang, G. Lu, S. Kang, F. Geng, B. Hu, *J. Phys. Chem. Lett.* **2023**, 14(20), 4682–4687.
- [14] J. Janek, W. G. Zeier, *Nat. Energy* **2016**, 1(9), 1–4.
- [15] CNBC, Solid Power, backed by Ford and BMW, begins pilot production of innovative EV battery with longer range and quicker recharging, Published Mon, Jun 6 **2022**. <https://www.cnbc.com/2022/06/06/solid-power-begins-pilot-production-of-solid-state-ev-battery.html>.
- [16] Electrive, QuantumScape prototypes 24-layer solid-state cells. Published Jul 29, 2022. <https://www.electrive.com/2022/07/29/quantumscape-prototypes-24-layer-solid-state-cells/>.
- [17] LICGC (AG-01) polished plates, Ohara Corporation. <https://www.ohara-inc.co.jp/en/product/licgca-01/>.
- [18] L. Katzenmeier, S. Helmer, S. Braxmeier, E. Knobbe, A. S. Bandarenka, *ACS Appl. Mater. Interfaces* **2021**, 13(4), 5853–5860.
- [19] L. Shen, J. Yang, G. Liu, M. Avdeev, X. Yao, *Mater. Today Energy* **2021**, 20, 100691.
- [20] P. Hartmann, T. Leichtweiss, M. R. Busche, M. Schneider, M. Reich, J. Sann, & J. Janek, *J. Phys. Chem. C* **2013**, 117(41), 21064–21074; J. Janek, *J. Phys. Chem. C* **2013**, 117(41), 21064–21074.
- [21] J. A. Lewis, J. Tippens, F. J. Q. Cortes, M. T. McDowell, *Trends Chem.* **2019**, 1(9), 845–857.
- [22] L. Katzenmeier, L. Carstensen, A. S. Bandarenka, *ACS Appl. Mater. Interfaces* **2022**, 14(13), 15811–15817.
- [23] A. Niemöller, P. Jakes, S. Kayser, Y. Lin, W. Lehnert, J. Granwehr, *J. Magn. Reson.* **2016**, 269, 157–161.
- [24] L. Katzenmeier, M. Gößwein, L. Carstensen, J. Sterzinger, M. Ederer, P. Müller-Buschbaum, A. Gagliardi, A. S. Bandarenka, *Commun. Chem.* **2023**, 6(1), 124.
- [25] S. A. Watzele, L. Katzenmeier, J. P. Sabawa, B. Garlyyev, A. S. Bandarenka, *Electrochim. Acta* **2021**, 391, 138969.
- [26] J. Kasemchainan, S. Zekoll, D. Spencer Jolly, Z. Ning, G. O. Hartley, J. Marrow, P. G. Bruce, *Nat. Mater.* **2019**, 18(10), 1105–1111.
- [27] L. Katzenmeier, M. M. M. Kaye, A. S. Bandarenka, *J. Electroanal. Chem.* **2022**, 922, 116750.
- [28] R. Götz, E. Pugacheva, Z. Ahaliabadeh, P. S. S. Llanos, T. Kallio, A. Bandarenka, *ChemSusChem* **2024**, e202401026.

Manuscript received: September 23, 2024

Revised manuscript received: October 6, 2024

Accepted manuscript online: October 29, 2024

Version of record online: November 16, 2024